Strong lensing reveals jets in a sub-microJy radio-quiet quasar

P. Hartley,[1]⋆ N. Jackson,[1] D. Sluse,[2] H. R. Stacey [ID][3,4] and H. Vives-Arias[5,6]

[1]*Jodrell Bank Centre for Astrophysics, School of Physics and Astronomy, University of Manchester, Oxford Road, Manchester M13 9PL, UK*
[2]*STAR Institute, Quartier Agora - Allée du six Août, 19c B-4000 Liège, Belgium*
[3]*ASTRON, Netherlands Institute for Radio Astronomy, Oude Hoogeveensedijk 4, NL-7991 PD Dwingeloo, the Netherlands*
[4]*Kapteyn Astronomical Institute, PO Box 800, NL-9700 AV Groningen, the Netherlands*
[5]*Instituto de Astrofísica de Canarias, Vía Láctea, s/n, E-38205 La Laguna, Tenerife, Spain*
[6]*Departmento de Astrofísica, Universidad de La Laguna, E-38205 La Laguna, Tenerife, Spain*

ABSTRACT

We present e-MERLIN and European VLBI Network observations which reveal unambiguous jet activity within radio-quiet quasar HS 0810+2554. With an intrinsic flux density of 880 nJy, this is the faintest radio source ever imaged. The findings present new evidence against the idea that radio-loud and radio-quiet quasars are powered by different underlying radio emission mechanisms, showing instead that the same active galactic nucleus (AGN) mechanism can operate as the dominant source of radio emission even in the very lowest radio luminosity quasars. Due to strong gravitational lensing, our source is not only visible, but with VLBI is imaged to a scale of just 0.27 pc: the highest ever resolution image of a radio-quiet quasar. Brightness temperatures of at least 8.4×10^6 K are associated with two highly compact components. Subsequent modelling of the lensed system has revealed that the components are linearly aligned on opposing sides of the optical quasar core, with the typical morphology of a compact symmetric object (CSO). Given that this source has been found to fall on the radio–FIR correlation, we suggest that the radio–FIR correlation cannot always be used to rule out AGN activity in favour of star formation activity. The correlation – or at least its scatter – may conceal the coexistence of kinetic and radiative feedback modes in AGN. Modelling of the lensing mass itself points to a non-smooth mass distribution, hinting at the presence of dark matter substructure which has manifested as astrometric perturbations of the VLBI lensed images.

Key words: gravitational lensing: strong – techniques: interferometric – galaxies: evolution – galaxies: jets – quasars: general – dark matter.

1 INTRODUCTION

The strong gravitational lensing of a background object results in the magnification of its size and, since surface brightness is conserved, its observed flux density [see Courbin, Saha & Schechter (2002), Meylan et al. (2006), and Bartelmann (2010) for extensive lensing reviews and formalism]. This powerful property allows us to use strong lenses as cosmic telescopes, typically increasing the effective sensitivity of the observing instrument to that of one 25–100 times bigger. With such a configuration we can make images of radio sources with nJy flux densities in a way that will only become routine with the Square Kilometre Array (Orienti et al. 2015). We can study these sources in more detail, resolving beam-limited structure into individual components (e.g. Claeskens et al. 2006; Jackson 2011). Strong lensing also results in the multiple imaging of

the background source, with typical image configurations consisting of either two or four magnified images in addition to a final, de-magnified image. Since the geometry of the resulting pattern is dependent only on the distribution of matter between the source and the observer, careful modelling of observations of strong lens systems can reveal the nature and amount of this matter, both baryonic and dark. At large scales, modelling of image separations allows us to measure the lensing galaxy profile (see e.g. Treu & Koopmans 2002, 2003, 2004; Sonnenfeld et al. 2012, 2013, 2015). At smaller scales, flux anomalies and image distortions allow us to probe galaxy substructure to look for evidence of dark matter sub-haloes (see e.g. Mao & Schneider 1998; Metcalf & Madau 2001; Kochanek & Dalal 2004; Vegetti et al. 2012; Nierenberg et al. 2017). With the exploitation of these remarkable science applications in mind, investigations have recently been conducted by Jackson et al. (2015), identifying the population of strongly lensed radio-quiet quasars (RQQs) as useful candidates for observation due to the sensitivity of their sub-mas brightness structure to small-scale grav-

⋆ E-mail: philippahartley@hotmail.com

itational perturbations, their relative insensitivity to microlensing effects, and their significant contribution to the number of lensed objects at the faint end of the radio luminosity function.

Although originally discovered in a radio survey (Schmidt 1963), most quasars actually produce relatively low levels of radio emission. The classic radio-loud quasar (RLQ) is typically observed to emit radio light from dramatic jets produced via the accretion of galactic gas and dust on to a central, supermassive, black hole. RQQs, on the other hand, are not associated with such obvious radio structure. The distinction between RLQs and RQQs is conventionally made using the ratio R of 5 GHz and optical B-band monochromatic luminosities, the cut being made at $R = 10$. While early optically selected samples found that most RQQs reside below $R = 1$ (Kellermann et al. 1989), source count studies undertaken by Blundell & Beasley (1998a) and Leipski et al. (2006) have found a less firm distinction between the two regimes, finding sources of intermediate flux density.

It is not known whether the radio emission that we do see in RQQs is due to the same active galactic nucleus (AGN) engine observed in RLQs, or whether starburst activity or other, more exotic, mechanisms are responsible. The possibilities have been debated extensively in the literature over several decades. Work by Condon et al. (2013) used a sample from the NVSS to show that there is an upturn in source counts at the faint end of the quasar luminosity function, hinting at a large population of star-forming sources residing at the μJy level. A simple 'unified' model based on AGN orientation has been ruled out by Kellermann et al. (2016), and some authors cite a lack of jet features as evidence for a lack of radio AGN activity (Padovani 2017). Herrera Ruiz et al. (2016), however, have shown using VLBA observations that the radio emission of at least some RQQs is dominated by an AGN, and Zakamska et al. (2015) have found that star formation rate in a sample of 300 quasars is insufficient to explain the observed radio emission, by an order of magnitude. Others point to the apparent flux density continuum, along with evidence of source variability by Barvainis et al. (2005), to argue for a model where the same AGN engine is operating – at differing levels of power – in each case. Alternative approaches to the problem have used the tight radio–far-infrared (radio–FIR) flux density correlation observed in star-forming regions (Sopp & Alexander 1991). White et al. (2017) showed an excess of radio emission compared to that expected from the radio–FIR correlation in a sample of QSOs, which cannot be explained by star formation alone. This result contradicted the findings of Bonzini et al. (2013, 2015). Optically thin bremsstrahlung emission in the core of the sources (Blundell & Kuncic 2007) and exotic mechanisms such as emission from magnetically heated coronae (Laor & Behar 2008; Laor, Baldi & Behar 2018) and radiatively driven shock fronts (Zakamska & Greene 2014) are also suggested.

By determining the RQQ radio emission process we will be able to address the wider problem of galaxy evolution, in particular the role of AGN feedback and whether AGN activity causes suppression or, alternatively, activation of star formation. Suspicion that the two processes are linked has arisen from evidence of corresponding trajectories over cosmic history (Madau & Dickinson 2014). However, it remains possible that the apparent connection is due simply to the same availability of gas over time. Many previous investigations have been statistical in nature and are subject to potential biases arising from sample selection. Additionally, some investigations have relied on the use of assumed spectral indices when converting catalogues of observed flux densities from one waveband to another. The use of observations of high resolution and

sensitivity, in combination with the magnifying power of lensing, allows us to avoid these problems and instead determine the nature of the radio structure by directly imaging it.

Radio observations of lensed quasars not only provide the magnification needed to expand our knowledge of the RQQ population, but also lend ideal conditions for the study of dark matter structure [see Zackrisson & Riehm (2010) and Jackson (2013) for recent reviews]. The 'missing satellite problem' describing the paucity of evidence for substructure (Klypin et al. 1999; Moore et al. 1999) persists, despite recent observations that have found some ultrafaint dwarf galaxies in proximity to our own (Belokurov et al. 2006; Zucker et al. 2006; Koposov et al. 2015; Homma et al. 2016) and a halving of the overall halo mass function predicted by the Illustris simutations (Graus et al. 2017). While observation of lensed extended sources can probe the higher mass end of the substructure mass function (10^9 M$_\odot$, Warren & Dye 2003; Dye & Warren 2005; Koopmans 2005; Vegetti et al. 2010, 2012; Ritondale et al. 2018), quasar lens systems provide a way of probing scales down to 10^6 M$_\odot$ (Mao & Schneider 1998).

Flux density perturbations due to small-scale structure, which can be betrayed by flux anomalies between merging images in cusp and fold configurations, have been observed in several lensed systems (see e.g. Fadely & Keeton 2012; MacLeod et al. 2013; Badole et al., in preparation). Radio observations of lensed quasars are particularly suitable for this study since, in the same manner as narrow-line regions (Nierenberg et al. 2017), microlensing events are likely to be rare. Unlike in the optical, where microlensing events occur frequently, only a single radio microlensing event has been observed to date (Koopmans et al. 2001). It is possible, however, that any flux density anomalies found in radio observations of lensed quasars could also be due to intrinsic AGN variability, scattering by galactic scintillation or intervening plasma clouds (see e.g. Phillips et al. 2000; Koopmans et al. 2003; Biggs 2004), the differential magnification of an extended background source (Serjeant 2012), or to disc and other baryonic structures within the lensing galaxy (Jackson et al. 1998; Moller, Hewett & Blain 2003; Xu et al. 2015; Hsueh et al. 2018). Astrometric perturbations of lensed images are harder to detect; several studies (Metcalf & Madau 2001; Chen et al. 2007; Zackrisson et al. 2013) predict offsets of just ∼1–10 mas between lens models containing a smooth mass distribution and those containing dark matter substructure. Such small perturbations can be revealed using the very high-resolution (∼1 mas) observations of Very Long Baseline Interferometry (VLBI), and attempts by Biggs et al. (2004) and Spingola et al. (2018) to fit smooth models to VLBI quasar observations have indeed struggled to obtain a satisfactory fit, strongly suggesting the presence of substructure in these examples. Sluse et al. (2012) have found, however, that small galaxies located within a few arcseconds of a lens but unaccounted for explicitly in the model can also produce astrometric anomalies of the order of a few mas.

In this paper we expand on the work of Jackson et al. (2015), who recently used the Karl G. Jansky Very Large Array (JVLA) and the extended Multi Element Remote Linked Interferometer Network (e-MERLIN) to detect a total of six strongly lensed RQQs. The observations implied an intrinsic lensed source flux density of just 1–5 μJy, constituting some of the very faintest radio sources ever detected. Two sources were subsequently detected at higher resolution using the e-MERLIN array. From this sample, we have selected QSO HS 0810+2554 for further investigation. Discovered by Reimers et al. (2002), HS 0810+2554 is a fold-configuration quad lens system with the source, a narrow-line quasar, at redshift $z = 1.51$ and a main lensing galaxy at an approximate redshift

of 0.89 (Mosquera & Kochanek [2011]). Jackson et al. ([2015]) have measured a spectral index for the radio emission of -0.55 ± 0.1, and have modelled the system to predict intrinsic sizes of the background radio source of <2 kpc and extended linearly. This scale, smaller than that typically observed in star-forming regions (Muxlow et al. [2005]; Wisnioski et al. [2012]), strongly suggests the presence of an AGN mechanism at play, producing radio emission from compact jet and core components. In the case of HS 0810+2554, the flux anomaly recorded in the optical was not apparent in the radio observations conducted by Jackson et al. ([2015]). For our study we have used the European VLBI Network (EVN) to investigate whether the compact structure predicted is in the jet/core form of an AGN or in the form of relatively diffuse starburst emission, invisible on the spatial scale of EVN baselines. We used the resulting radio map to model the lens mass distribution and reconstruct the background source. We present imaging and modelling results from this observation, alongside further observations made using e-MERLIN.

2 OBSERVATIONS AND CALIBRATION STRATEGY

2.1 EVN observation

Radio continuum observations of HS 0810+2554 were carried out on 2016 March 3 and 2016 March 4 using the EVN (projects EJ016A and EJ016B) at 1.6 GHz, over a frequency range of 1539–1667 MHz. The total bandwidth was divided into eight adjacent spectral windows, each divided into 32 channels and a visibility integration time of 2 s was used. A total of 14 telescope dishes were combined into a synthesized aperture, spanning baseline lengths up to 7000 km to achieve a beam-limited resolution of the order 0.001 arcsec. A nearby point source, J 0813+2435, was observed in order to obtain phase corrections. 4C39.25 was observed in order to adjust for the bandpass. The largest dish, Effelsberg, was only available for one of the two days of observation.

Data were initially reduced using the EVN pipeline, which uses a PARSELTONGUE wrapper to perform calibration and imaging routines from the Astronomical Image Processing System (AIPS) software package distributed by NRAO (Greisen [2013]). Fringe fitting was performed to remove instrumental and atmospheric delay, using observations of the phase calibrator and bandpass calibrator. Inspection of delay solutions revealed long delays induced at the 76m Lovell telescope at Jodrell Bank during the first epoch, which, due to long intervals between phase referencing necessitated by long slew times, resulted in an incorrect interpolation of delay solutions for baselines to this antenna. Data containing the Lovell were therefore lost for half of the total observation time. Phase and amplitude calibration was also performed using the phase calibrator with a point source model, and the solutions transferred to the target source. Pipeline solutions were refined by carrying out additional flagging of radio-frequency interference (RFI) and by performing additional manual self-calibration on the phase calibrator. Self-calibration of the target source was attempted but solutions were unstable due to a small number of larger antennas dominating the signal, despite experiments which downweighted these stations. Final maps were produced using three different weighting strategies, ranging from fully natural weighting, which maximizes sensitivity, to a compromise weighting between natural and uniform, which modifies the weights of individual visibilities by their local density in the u–v plane, upweighting longer baselines to increase resolution.

2.2 e-MERLIN observations

Radio observations of HS 0810+2554 were carried out using the e-MERLIN array at about 5 GHz (*C* band). The 76m Lovell dish – the largest of the array – was not available for this study. Three 24 h observations were performed, each at a different 512 MHz bandwidth within the tunable *C* band range of 4–8 GHz. Each 24 h observation was performed across three epochs, resulting in a total of nine visibility sets for calibration and imaging. Observations on 2015 December 14 and 15 and 2016 February 28 used a frequency range centred on 5.12 GHz, on 2016 May 12–14 used 4.32 GHz, and on 2016 May 15–17 used 7.12 GHz. Each epoch used an integration time of 1 s and the total bandwidth was divided into four IFs, each further divided by a channelization of 512, resulting in channels 0.25 MHz wide. Phase referencing was performed using the nearby bright point source J 0813+2435, 3C 286 was observed in order to set the flux scale, and the bright point source OQ208 was used to calculate the bandpass response.

Data reduction followed standard procedure (Argo [2015]), again using the AIPS package. Initial inspection of the visibility data showed significant RFI contributions and antenna dropouts variously affected different antennas and calibrator sources. Additionally, the Defford antenna – known to have low sensitivity at *C* band – showed little signal over the background noise during the last six epochs, with too much scatter to determine an accurate phase slope in the frequency domain. These data from this telescope was therefore discarded from the 4.32 GHz and 7.32 GHz observations. After performing nominal delay subtraction by fringe-fitting the data from all calibration sources, separate complex gain calibration was performed, followed by bandpass calibration and the setting of the overall flux scales. Gain solutions for the phase reference source were refined using self-calibration with a point source model, and solutions transferred to the the target. The described procedure was performed individually for each epoch, before the visibility data of epochs of matching frequency were combined for imaging and further calibration.

Self-calibration of the faint target was aided by the presence of a $\sim$200 µJy confusing source located close to the edge of the usable field of view (F.o.V.), 6 arcmin from the pointing centre. Using a point source model for this source resulted in a significant refinement of residual phase errors arising from atmospheric instabilities in the vicinity of the target, improving the dynamic range considerably in the 5.1 GHz and 4.32 GHz maps. The technique relied on the use of unaveraged visibility data in order to avoid significant smearing of the confusing source. Unfortunately, smearing resulting in $\sim$30 per cent intensity loss could not be avoided in the 7.32 GHz map, and self-calibration was not successful in this case. Final maps were produced using natural weighting.

3 RADIO MAPS

3.1 EVN map

The naturally weighted EVN image of 0810+2554 is shown in Fig. [1]. The off-source r.m.s. noise level is 7 µJy. The image shows a clear detection of the lensed RQQ, with several components visible over $5\sigma_{\text{r.m.s.}}$. A total of eight lensed components are identified, indicating that the EVN has resolved the extended background structure observed by e-MERLIN at *L* band into two separate components, here referred to as source 1 and source 2. In order to correctly associate components of the lensed image with components of the background source, the modelling process
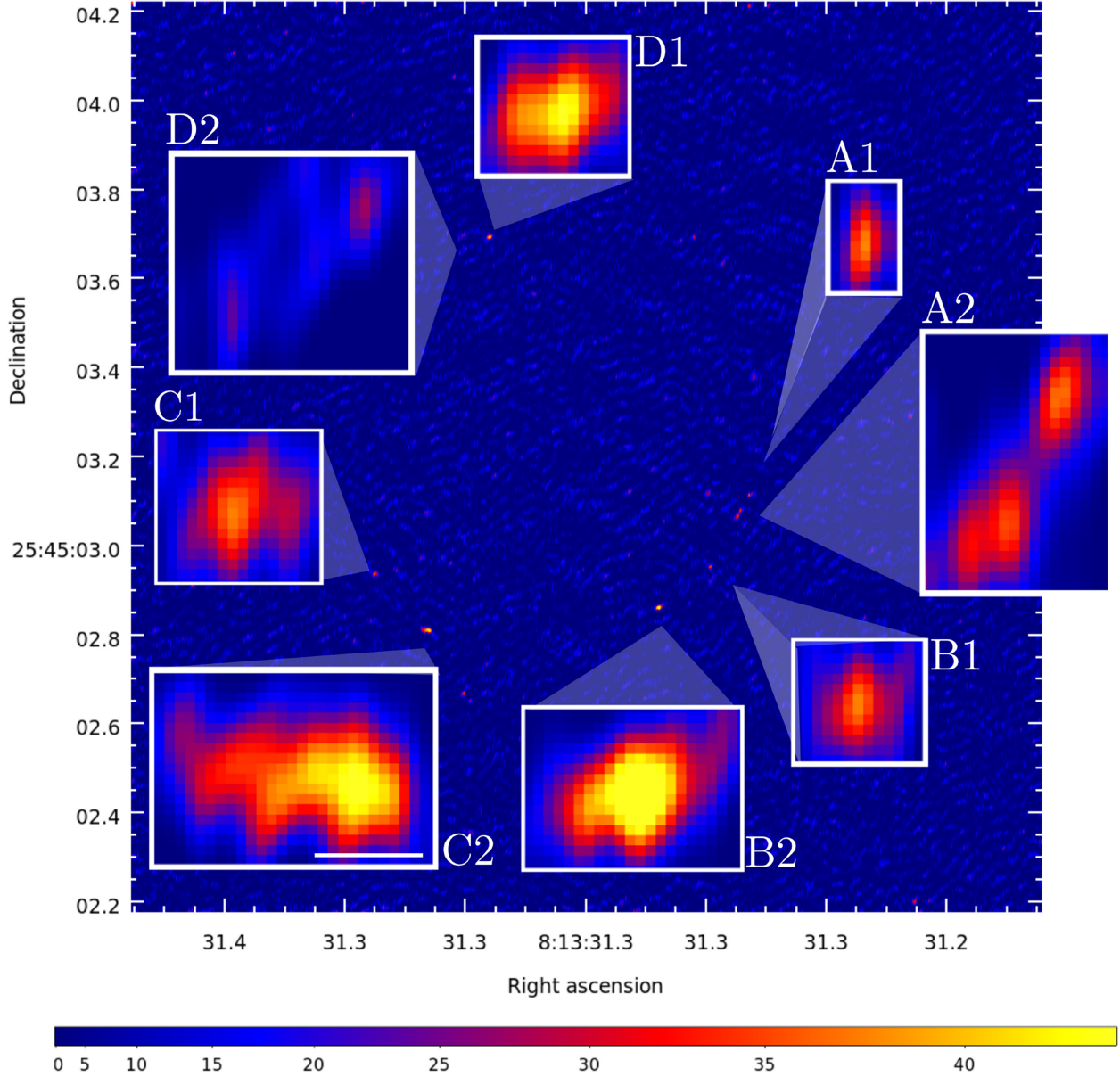
Figure 1. EVN image of HS 0810+2554 at 1.65 GHz produced using a natural weighting scheme. The peak surface brightness is 52 μJy beam^{-1}, at component B2. The beam is at full width at half-maximum (FWHM) at 12.0 × 8.5 mas at a position angle of −3°. We use the nomenclature of Reimers et al. (2002) for respective pairs of components associated with background sources 1 and 2. A contour plot of the uncovered background is supplied in A1.

discussed in Section 4 was iterated over all combinations of four pairs within the total of eight lensed components. This revealed a clear preference for the configuration notated in Fig. 1, with a five-fold improvement in goodness-of-fit over the second-preferred configuration.

The maps produced using the two mixed weighting schemes provide additional insight into the nature of the two background sources. Fig. 2 displays each component image using restoring beam sizes of 12.0 × 8.5 mas, 12.8 × 4.0 mas, and 11.1 × 3.4 mas for weighting schemes which used a Briggs' robustness parameter of 5, 1, and 0, respectively. As increasingly higher resolution is used, components A2, B2, and C2 become distinctly resolved into two separate unresolved subcomponents. In the map using the highest resolution, all components in the map are completely unresolved, suggesting that the two background sources are both

highly compact. Flux density measurements for all components at all resolutions were made using AIPS task JMFIT, which fits Gaussian components to the sky brightness distribution. A double Gaussian model was used to fit the flux density components belonging to source 2, and a single Gaussian used for source 1. The results, along with associated errors, are reported in Table 1.

The flux density measurements were used in order to place a lower limit of the brightness temperatures of the radio components in the source plane. According to the Rayleigh Jeans law, the brightness temperature, T_B, of a non-thermal source can be written:
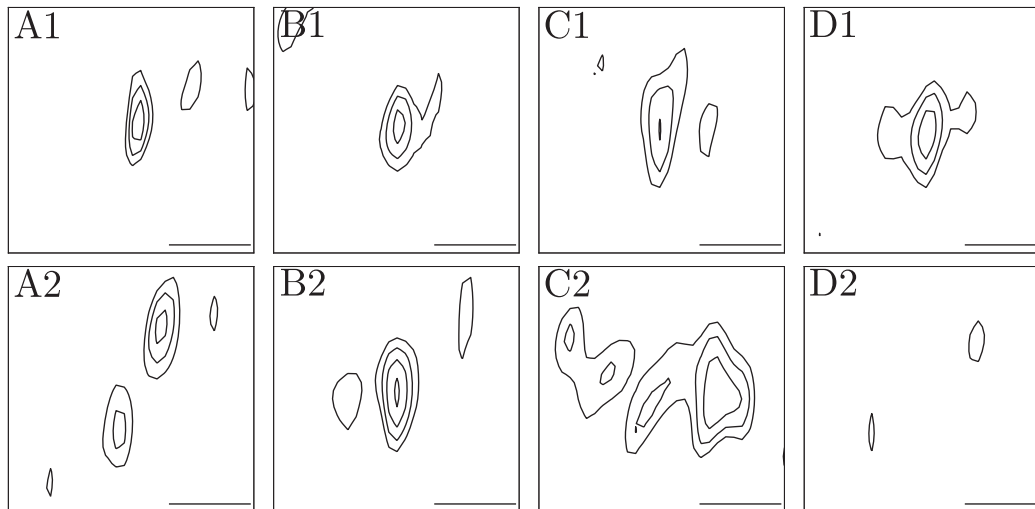
$$T_B = 1222 \times \frac{I}{\nu^2 \theta_{\mathrm{maj}} \theta_{\mathrm{min}}}, \tag{1}$$

where ν is the observing frequency in GHz, θ_{maj} and θ_{min} are the half-power beam widths along the major and minor axes,

(a) Components imaged using a restoring beam FWHM of 12×8.5 mas.
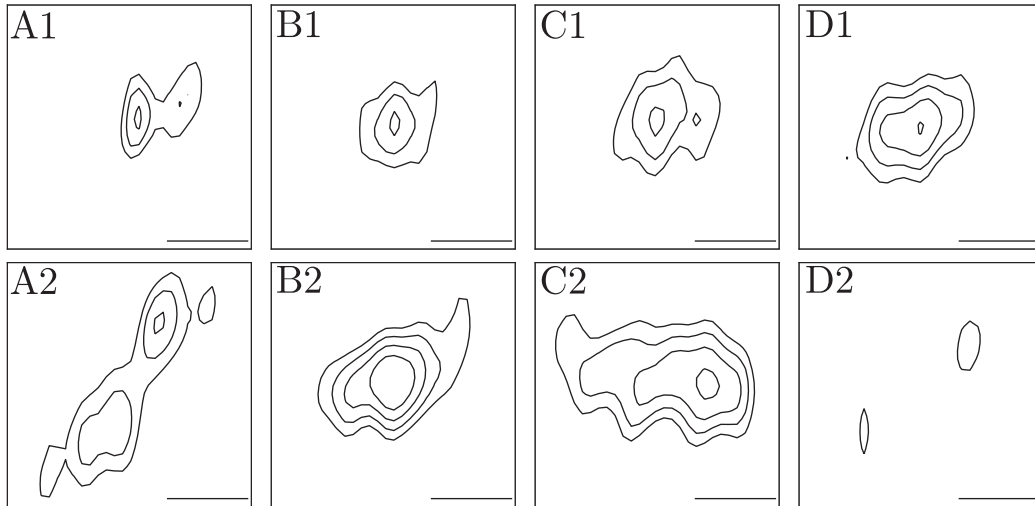
(b) Components imaged using a restoring beam FWHM of 12.8×4.0 mas.

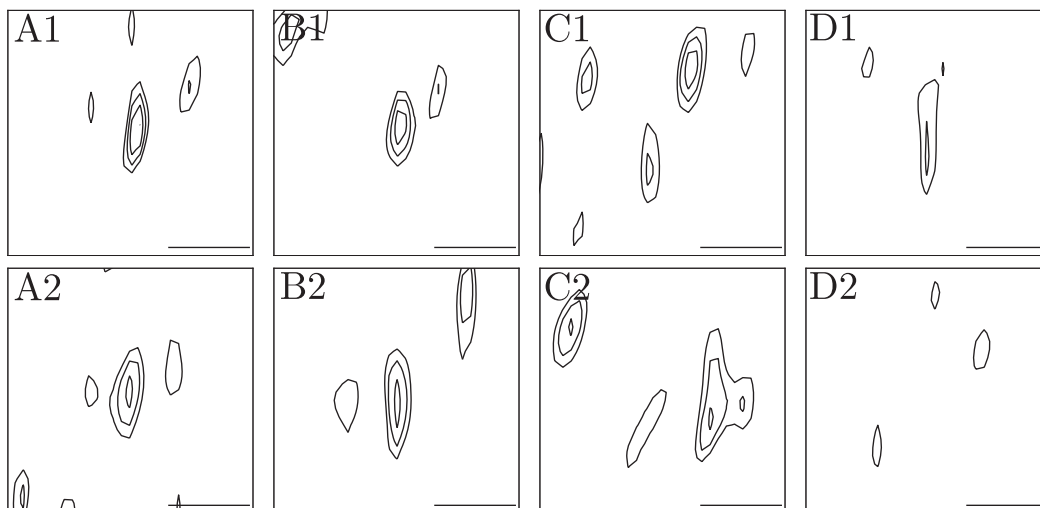(c) Components imaged using a restoring beam FWHM of 11.1×3.4 mas

Figure 2. Maps of the lensed components of HS 0810+2554 made using three different weighting schemes, from a natural weighting scheme (top) to a compromise weighting scheme between natural and uniform (bottom), with robustness parameters of 5, 1, and 0 in the Briggs' weighting scheme, respectively. In all images contours have been drawn at $(-3, 3, 4, 5, 6) \times 7.2$ μJy and the scalebar represents a length of 10 mas.

Table 1. Radio flux density measurements made in μJy of the components of HS 0810+2554 observed with the EVN at 1.65 GHz. Measurements of each component were taken from images made using three different weighting schemes, from a natural weighting scheme to a compromise weighting scheme between natural and uniform, with robustness parameters of 5, 1, and 0 in the Briggs' weighting scheme, respectively. The values corresponding to source 2 were measured by fitting two Gaussian components, a and b, in each case. Errors are derived from AIPS task JMFIT and do not include an uncertainty on the setting of the overall flux density scale 5–10 per cent.

Component	12×8.5 mas	12.8×4.0 mas	11.1×3.4 mas
A1	37 ± 7	39 ± 8	44 ± 9
A2a	35 ± 7	38 ± 8	37 ± 8
A2b	32 ± 7	27 ± 8	24 ± 8
B1	32 ± 7	35 ± 9	37 ± 8
B2a	52 ± 7	39 ± 8	45 ± 9
B2b	41 ± 7	21 ± 8	29 ± 9
C1	35 ± 7	35 ± 8	35 ± 8
C2a	45 ± 7	41 ± 8	41 ± 8
C2b	34 ± 7	29 ± 8	31 ± 8
D1	43 ± 7	46 ± 8	41 ± 9
D2a	20 ± 7	25 ± 9	27 ± 9
D2b	20 ± 7	21 ± 8	22 ± 9

respectively, measured in arcseconds, and *I* is the source brightness intensity measured in mJy beam^{-1}. At an observing frequency of 1.65 GHz, and with a restoring beam of $\theta_{\mathrm{maj}} = 11.1$ and $\theta_{\mathrm{min}} = 3.4$ mas, the measurements of flux density per beam from Table 1 give maximum values of 0.045 ± 0.009 mJy and 0.044 ± 0.009 mJy for source 1 and source 2, respectively. According to AIPS task JMFIT, the sources are unresolved in all lensed components at this resolution. Since a source is considered to be unresolved if its deconvolved FWHM size is smaller than one-half the synthesized beam FWHM, and since the lensed components are magnified in orthogonal directions, we assume an upper limit to the physical source size of $\theta_{\mathrm{maj}} = 1.55$ mas and $\theta_{\mathrm{min}} = 1.55$ mas, using half the value of the beam size as is conventional for radio-continuum observations (e.g. Mundell et al. 2000; Ulvestad & Ho 2001; Miettinen et al. 2017). Brightness temperatures of $8.4 (\pm 0.3) \times 10^6$ and $8.2 (\pm 0.3) \times 10^6$ K therefore represent lower limits. Using the spectral index determined using our e-MERLIN observation below, the *K*-corrected flux densities in the $z = 1.51$ rest frame of the source yield brightness temperatures of at least $6.0 (\pm 0.6) \times 10^6$ and $5.8 (\pm 0.5) \times 10^6$ K.

3.2 e-MERLIN maps

Final e-MERLIN maps observed at 4.32 and 5.12 GHz are shown in Fig. 3. The 7.32 GHz map, which suffered both from the loss of the Defford station and from the lack of self-calibration on the target, showed no detection of the source. In order to allow direct comparison between the two frequencies, both maps were produced using the same circular restoring beam of 70×70 mas. In the 5.12 GHz map component C is resolved into the two subcomponents seen in the EVN map, but is not prominent within the higher noise of the 4.32 GHz map. Flux density measurements for all components in each map were again obtained using JMFIT. The results are presented in Table 2. There is no evidence of a flux anomaly between images A and B in either map. A relatively steep spectral index of $\alpha = -0.63 \pm 0.14$ was calculated using flux density measurements at component A, in agreement with the measurement made by Jackson et al. (2015).

3.3 All radio photometric data

Fig. 4 presents all recorded flux density measurements for HS 0810+2554. Since interferometry is sensitive to the spatial scale determined by the size of the beam, any loss of flux density with an increase in resolution implies that at least some of the source occupies an angular extent up to and including the larger beamsize. By accounting for the spectral index obtained from our e-MERLIN observations, we find a flux density loss of 37 (± 4) per cent with a beamsize reduction from 300×240 mas at 1.4 GHz to 12.0×8.5 mas at 1.65 GHz, when using the summed flux density from all components in each case. While most of the signal is contained within the very compact extent of the VLBI beam, some signal appears to originate from more diffuse structure.

Our analysis does not account for any intrinsic variation of the source flux density or position. Particularly on the time-scales between the observations by Jackson et al. (2015) and our own observations, quasar radio emission resulting from AGN activity has been observed to vary. Variation has even been detected within the few months difference in arrival times between components of this lens system (Blundell, Beasley & Bicknell 2003; Berdina & Tsvetkova 2018). Additionally, millilensing by dark matter sub-haloes can play a role, resulting in flux density variation over time if placed in front of a moving jet. For example, subhalo masses of 10^6 yield Einstein radii of ~ 1 mas (Mao & Schneider 1998), which could be traversed by a distant relativistic jet within a time-scale of just ~ 1 yr in a typical quad lens system with modest magnification of the source plane. Either or both of these effects could be responsible for the variation in flux ratios of the more separated components from epoch to epoch, and could also contribute to the apparent spectral index.

4 LENS MODELLING

4.1 Methodology

After revealing a clear detection of HS 0810+2554 at VLBI resolution, the EVN map was used to model the lens mass distribution and reconstruct the background source. Modelling software was written in PYTHON. The script models the lens as a single isothermal ellipse (SIE) plus external shear and performs inverse ray tracing, populating the image plane with surface brightness values from the source plane. This is achieved by evaluating the deflection by the lensing mass at each point in the image plane and assuming a thin lens approximation. The source itself was modelled as a set of two two-dimensional Gaussian components.

In total, a set, Θ, of 11 free parameters were used to produce the model: source positions SX1, SY1 and SX2, SY2; lensing galaxy position and major axis, GX, GY and Gb; lensing galaxy ellipticity and position angle, GE and GPA; and external shear magnitude and position angle, GSM and GSA. The position of the lensing galaxy could not be fixed since it was undetected in the EVN image. Due to the point morphology of the lensed images, the ellipticity of the source components was set to zero, and their sizes to a nominal circular value. Since there is a degeneracy between the ellipticity of the SIE and the external shear, two approaches were attempted. First, the best model which used all 11 parameters was obtained. This model showed bimodal distributions for both the lensing galaxy ellipticity and the shear magnitude, confirming the anticipated degeneracy and resulting in artificially large uncertainty values for these parameters. In order to determine these parameters and their uncertainties in the absence of degeneracy, another model was
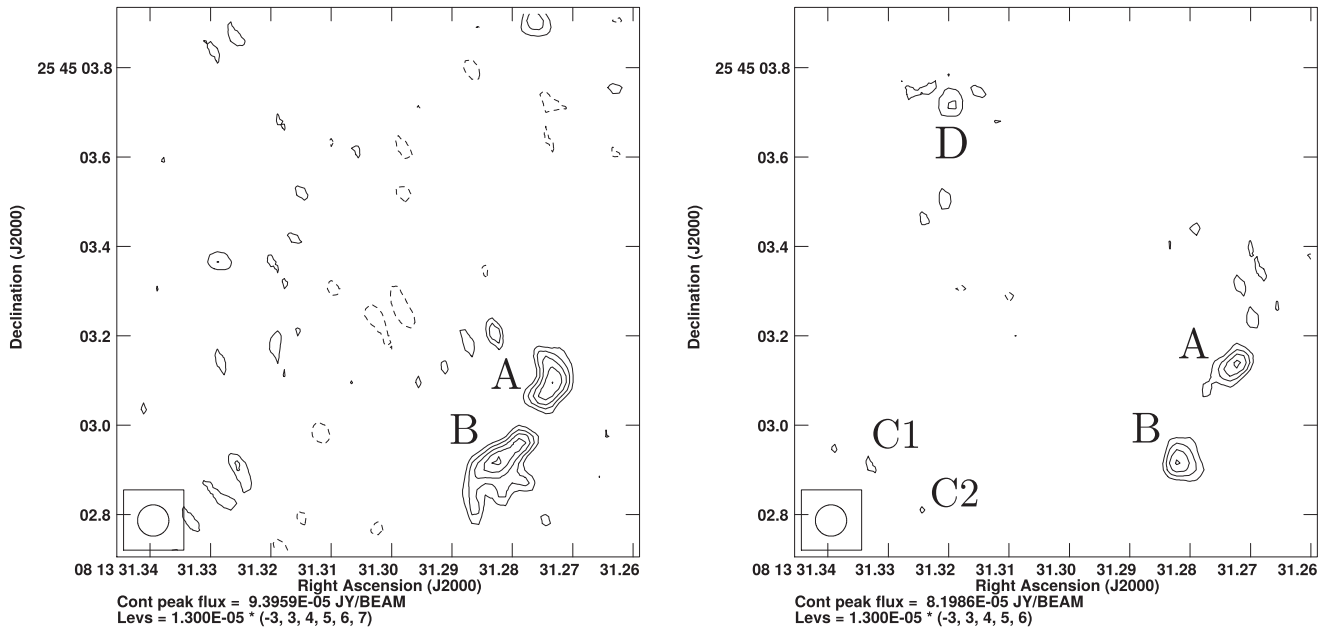
Figure 3. Maps of HS 0810+2554 made from e-MERLIN observations at 4.32 GHz (left) and 5.12 GHz (right). Both maps were produced using the same 70 × 70 mas restoring beam. Both maps also use the same contouring scheme, at values of $(-3, 3, 4, 5, 6, 7) \times 13$ μJy, which is the value of the off-source r.m.s. noise in the higher sensitivity 5.12 GHz map. The image components with signal higher than the respective value of $3\sigma_{\text{r.m.s.}}$ in each map are labelled.

Table 2. Radio flux density measurements made in μJy of the components of HS 0810+2554 observed with the e-MERLIN at 4.32 and 5.12 GHz. Errors are derived from AIPS task JMFIT and do not include an uncertainty on the setting of the overall flux density scale of 5–10 per cent.

Component	4.32 GHz	5.12 GHz
A	93.7 ± 18.8	82.0 ± 12.7
B	91.3 ± 18.8	80.0 ± 12.7
C1	46.9 ± 18.8	42.1 ± 12.7
C2	43.7 ± 18.8	46.0 ± 12.7
D	43.1 ± 18.8	53.5 ± 12.7

obtained by first finding the best model without external shear and then fixing the SIE mass and ellipticity to leave only external shear and position angle to vary, as suggested by Keeton, Kochanek & Seljak (1997). This model resulted in a better fit to observations.

Due to the point source nature of the lensed source, the objective function was constructed to measure a χ^2 based on the positions of the eight lensed image components, driving the optimizer to find the model which would produce the minimum distances between the positions $\mathbf{x}^{\text{obs}}$ of the observed components and positions $\mathbf{x}(\Theta)$ of the model components, and penalizing outliers:

$$\chi^2 = \sum_i^N \frac{|\mathbf{x}_i^{\text{obs}} - \mathbf{x}_i(\Theta)|^2}{\sigma_i^2}, \qquad (2)$$

where N is the number of image components to be used to constrain the model and σ is the error on the position of each component i. Due to the possibility of intrinsic source variation, flux density values were not used as constraints to the model. As found by Garrett et al. (1994) and Rusin et al. (2002), the relative astrometry of the lensed components can constrain the components of the relative magnification tensors without needing to use any flux density information. Modelling in the u–v plane of the interferometric data was not attempted, since the EVN provides good u–v coverage, despite the absence of two telescopes for half of the observing time.
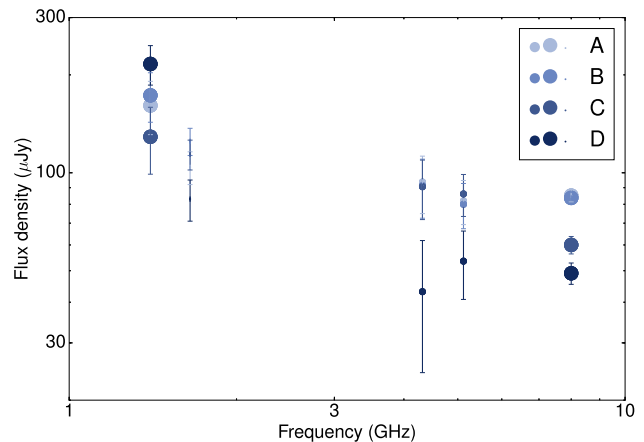

Figure 4. Radio spectral energy distribution of HS 0810+2554, constructed using our EVN 1.65 GHz and e-MERLIN 4.32 GHz and 5.12 GHz observations, and the VLA 8 GHz and e-MERLIN 1.4 GHz observations made by Jackson et al. (2015). The size of the circles is proportional to the beamsize used in each observation.

We performed another model fit using the optical relative astrometric positions from *HST* observations from the CASTLES data base (Kochanek et al. 1999) as additional constraints, adding two further parameters, SX3 and SY3, to the model. This allowed us to reconstruct both the radio and optical components simultaneously in the source plane. Given that the absolute astrometric uncertainties available for *HST* data are larger than those obtained using the EVN, the absolute astrometric positions of the *HST* components were not used as a constraint to the model. Instead, the *HST* component positions were overlaid on to the EVN component positions in a 'best guess' by eye. The optical source was then modelled by constructing a second SIE with a variable position, GX2 and GY2, but with a mass distribution fixed to the same values as the first

Table 3. The best-fitting, mean, and uncertainty on the mean are presented for the parameters of the maximum-likelihood models of HS 0810+2554 obtained using positional constraints from the EVN image only and the EVN image plus the *HST* positions from the CASTLES data base (Kochanek et al. 1999). The fitting was performed using the MULTINEST Bayesian sampling tool. Galaxy and source positions are reported with respect to lensed imaged A1. Since absolute astrometric uncertainty associated with the *HST* image positions is larger than the absolute astrometric uncertainty associated with the EVN positions, *HST* absolute astrometry was not used as a constraint. Instead, the whole *HST* system was initially placed at a nominal 'best guess' position with respect to the EVN system. A model was then constructed to contain two identical SIEs, one for each system. After convergence, the whole *HST* system was shifted by the difference between the best-fitting positions of the two lensing galaxies, i.e. GX-GX2 = 24.1 and GY-GY2 = −6.4 in order to align the *HST* SIE with the EVN SIE, and to determine the respective locations of radio and optical components in the source plane (Fig. 6). The positions of the *HST* galaxy and source are quoted before performing this shift, in order to report the respective uncertainties.

| Parameter code	Parameter name	EVN only			EVN+*HST*		
		Mean	Sigma	Best fit	Mean	Sigma	Best fit
GX	Galaxy RA/mas	474.8	2.3	474.0	474.9	0.5	474.6
GY	Galaxy Dec./mas	142.9	5.93	135.2	137.72	1.4	138.6
SX1	Source 1 RA /mas	477.6	2.4	476.4	477.4	0.5	477.3
SY1	Source 1 Dec./mas	124.8	3.2	123.0	122.6	1.2	123.42
SX2	Source 2 RA /mas	467.2	2.5	469.2	468.7	0.7	468.2
SY2	Source 2 Dec. /mas	119.4	2.8	119.0	117.9	0.9	118.6
GB	Einstein radius along major axis/mas	477.6	2.3	475.4	479.1	0.7	479.5
GE	Galaxy ellipticity	0.110	0.020	0.077	0.094	0.0018	0.094
GPA	Galaxy PA/°	23.4	0.3	23.2	23.3	0.1	23.3
GSM	External shear	0.0003	0.0002	0.0001	–	–	–
GSA	External shear PA /°	126.7	43.6	29.0	–	–	–
GX2	HST galaxy RA/mas	–	–	–	451.0	1.8	450.5
GY1	HST galaxy Dec./mas	–	–	–	145.0	1.9	145.0
SX3	HST source RA /mas	–	–	–	450.2	1.7	449.8
SY3	HST source Dec./mas	–	–	–	128.1	1.9	128.1
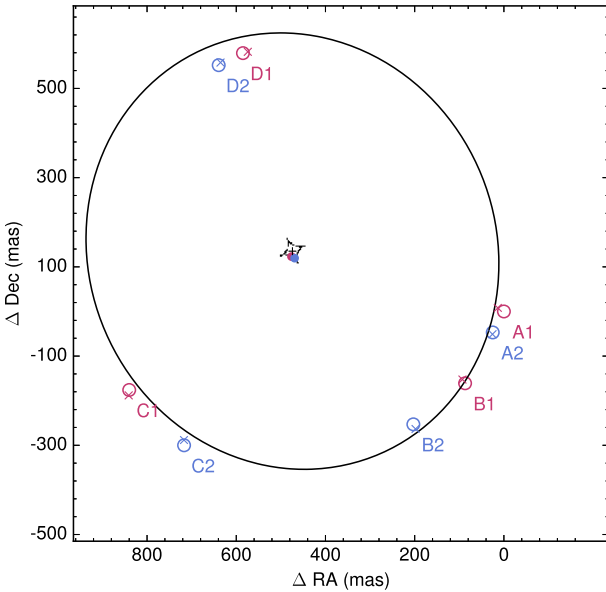
Figure 5. The best-fitting model of HS 0810+2554 obtained using the positions of components in the EVN image as constraints. The lensing galaxy was modelled as an SIE and is centred on the vertical cross. The model includes a very small amount of external shear. The tangential critical curve is represented by the thin black curve and the caustic by the thick black curve. The predicted positions (crosses) of lensed components are plotted for comparison with observed component positions (open circles). The predicted positions of the components in the source plane (filled circles) are also plotted. Source 1 is represented by red markers and source 2 by blue. The model parameters and uncertainties are reported in Table 3 and derived parameters in Table 4. The model and observed component positions are reported in Table 5. All positions are plotted with respect to component A1.
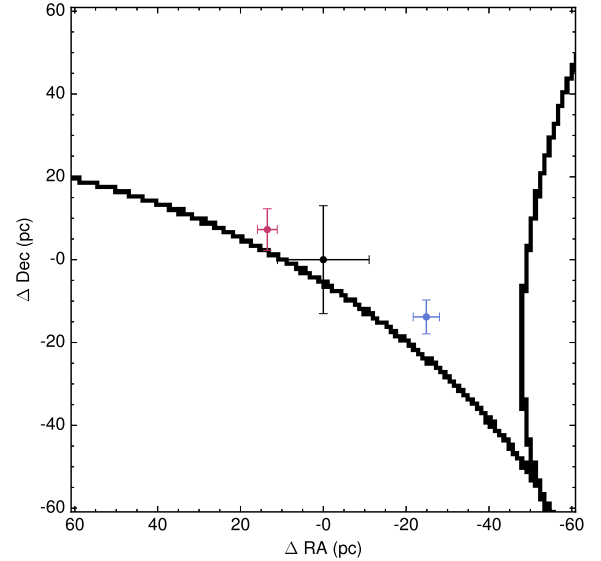
Figure 6. Reconstruction of the lensed sources within the tangential caustic curve using both *HST* (black) positions and VLBI (blue and red) positions from the best-fitting EVN+*HST* model. Uncertainties (listed in Table 1) were obtained from the MULTINEST Bayesian sampling tool and are represented at 1σ by the error bars. The components are plotted in the source plane at $z = 1.51$, assuming a standard flat cosmology with $\Omega_m = 0.27$ and $H_0 = 68$ km s^{-1} Mpc^{-1}.

SIE. Optical lensed image positions constrained the position of the second SIE which was shifted – along with the relative positions of the optical lensed image positions and the relative position of the background optical source – to the same position as the first SIE
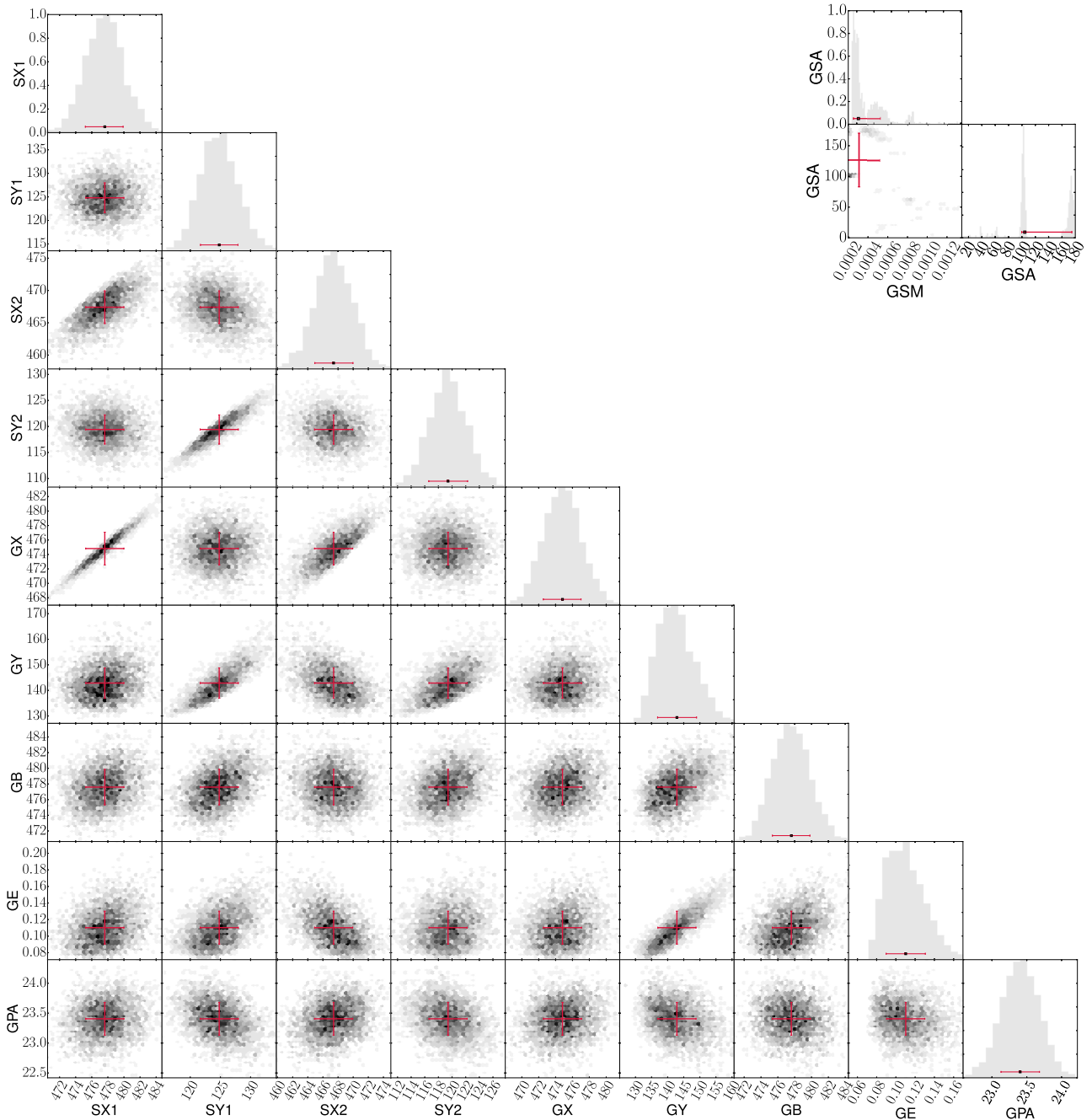
Figure 7. Posterior PDF plots for the parameters of the best-fitting model of HS 0810+2554. In each plot the error bars are centred on the mean and extend to the 3σ uncertainty values in the two-dimensional plots and to 1σ in the one-dimensional plots. This model was obtained after first fitting for source positions and SIE mass model and position only, before then fixing the best-fitting values of these parameters and allowing only external shear magnitude and angle to varying. The PDF plots are therefore separated into these two sets of parameters. This procedure avoided a degeneracy between lens ellipticity and external shear.

Table 4. Additional properties of the system. The source properties are derived from the best-fitting parameters of Table 3 for the model fit using EVN positional constraints only. The source centroid position is quoted with respect to the galaxy position.

Density slope (2 ≡ isothermal)	≡2.0
Source separation /mas	8.2 ± 6.2
Source position angle /°	60.9 ± 23
Source centroid position /mas	2.8 ± 3.1 W, 14.2 ± 6.1 S

once model convergence was reached. Due to the growing parameter space, for this model we only performed a fit without external shear.

Bayesian inference, a probabilistic method that has been applied to several model-fitting problems in strong and weak lensing (Suyu et al. 2006; Jullo et al. 2007; Miller et al. 2007), has been used to derive the probability distribution function (PDF) associated with the model parameters. Sampling of the parameter space was performed using the MULTINEST (Feroz & Hobson 2008; Feroz, Hobson & Bridges 2009; Feroz et al. 2013) method implemented

Table 5. Observed and modelled positions for each lensed component of HS 0810+2554. All positions are measured with respect to component A1 in the EVN image. The observed *HST* positions were set to a nominal reference position prior to model fitting, so that the difference between EVN lensing galaxy position, GX and GY, and *HST* lensing galaxy position, GX2 and GY2, was effectively a free parameter in the fit. After model convergence the quoted observed and predicted positions were then shifted by this difference, GX-GX2 = 24.1 and GY-GY2 = −6.4 (using the best-fitting positions from Table 3), in order to view the relative physical positions of all components in Fig. 8.

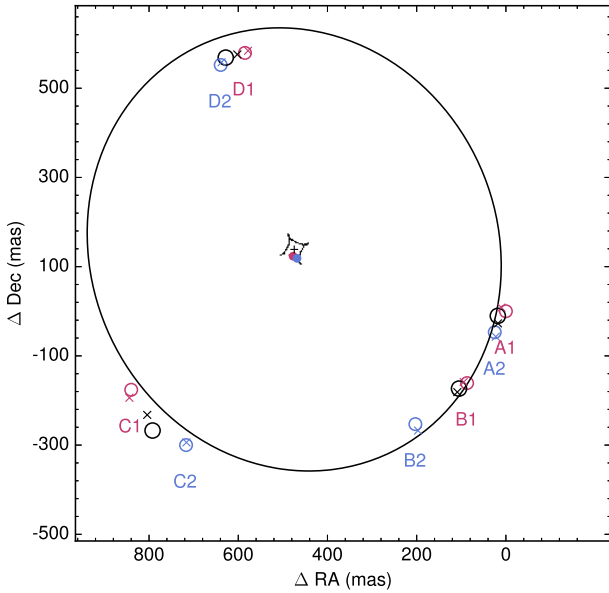| | Observed | | Modelled | | | |
| | | | EVN only | | EVN+*HST* | |
Comp.	ΔRA (mas)	ΔDec. (mas)	ΔRA (mas)	ΔDec. (mas)	ΔRA (mas)	ΔDec. (mas)
A1	0.0 ± 1.4	0.0 ± 1.0	13.5	8.1	9.9	8.2
A2	25.8 ± 1.2	− 47.2 ± 1.5	25.6	− 50.9	22.5	− 57.0
B1	87.5 ± 1.2	− 161.8 ± 0.8	93.0	− 152.6	94.5	− 158.4
B2	203.4 ± 1.0	− 253.4 ± 1.0	198.0	− 263.4	197.0	− 267.4
C1	840.5 ± 1.6	− 176.3 ± 1.2	841.2	− 187.6	844.0	− 194.0
C2	717.9 ± 1.5	− 300.1 ± 0.9	717.2	− 288.2	716.2	− 293.9
D1	585.1 ± 1.3	579.9 ± 1.3	574.0	582.0	578.0	584.0
D2	640.6 ± 4.1	552.2 ± 2.1	635.3	558.0	637.4	558.3
A *HST*	− 6.0 ± 5	− 4 ± 5	–	–	− 6.4	− 20.8
B *HST*	87.0 ± 5	− 167.0 ± 5	–	–	84.9	− 174.9
C *HST*	794 ± 5	− 261 ± 5	–	–	780.1	− 225.9
D *HST*	604 ± 5	575 ± 5	–	–	578.0	582.0

Figure 8. The best-fitting model of HS 0810+2554 obtained using the positions of components in the EVN image and *HST* observations as constraints. The lensing galaxy was modelled as an SIE and is centred on the vertical cross. The tangential critical curve is represented by the thin black curve and the caustic by the thick black curve. The predicted positions (crosses) of lensed components are plotted for comparison with observed component positions (open circles). The predicted positions of the components in the source plane (filled circles) are also plotted. Source 1 is represented by red markers, source 2 by blue, and the source observed by *HST* in black. Model parameters and uncertainties are reported in Table 3 and derived parameters in Table 4. Model and observed component positions are reported in Table 5. All positions are plotted with respect to component A1.

in PYTHON using the PYMULTINEST (Buchner et al. 2014) package. Uniform priors ranging over 100 mas in each case were used for galaxy (GX2 = 450–550, GY2 = 100–200, GX2 = 450–550, GY2 = 100–200) and source positions (SX1 = 450–550, SY1 = 100–200, SX2 = 450–550, SY2 = 100–200, SX3 = 450–550, SY3 = 100–200), and galaxy major axis (GB = 450–550). Flat priors

were used for galaxy and shear position angles, while logarithmic priors were used for galaxy ellipticity and shear magnitude. In order to reduce computation time, image resolution was downsampled by a factor of 2.

4.2 Results

The parameter values from the best-fitting model using the EVN positional constraints only are presented in Table 3 and plots of the marginalized probability densities in Fig. 7. The derived values are presented in Table 4. Predicted lensed image positions are compared with observed positions in Table 5 and plotted in Fig 5, along with source and galaxy positions and the extent of the tangential critical and caustic curves. Using positional errors from Table 5, the model represents an imperfect fit, suggesting astrometric perturbations arising from substructure along the line of sight. A fit of $\chi^2_{\rm red} = 1$ is only achieved by relaxing the RA and Dec. positional constraints of the EVN image to within ±8 mas for the model containing a fixed external shear magnitude of zero, or to within ±9 mas when external shear is allowed to vary. The poorer fit after the addition of shear reflects the reduction in degrees of freedom combined with the low value of shear predicted. More detailed mass modelling of astrometric anomalies arising from possible substructures along the line of sight will be presented in a forthcoming paper.

The parameter values of the best-fitting model are in reasonable agreement with the model produced by Jackson et al. (2015) (hereafter J15), the values of which were not used as priors or constraints to the VLBI model. The galaxy critical radius, the source centroid position, and the source position angle – defined as the angle of orientation between the background source components – all agree to within 1σ. Galaxy ellipticity and external shear do not agree, while our model predicts a minimal external shear value and significant galaxy ellipticity, the model of J15 predicts the opposite. This can be explained by the degeneracy between the two forms of lensing distortion (Kochanek 2004). This was borne out during the modelling process, which found complementary, bi-modal, distributions in the marginal plots of galaxy ellipticity and external shear when both parameters were searched over simultaneously. The shear position angle of J15 agrees to just outside 1σ of the
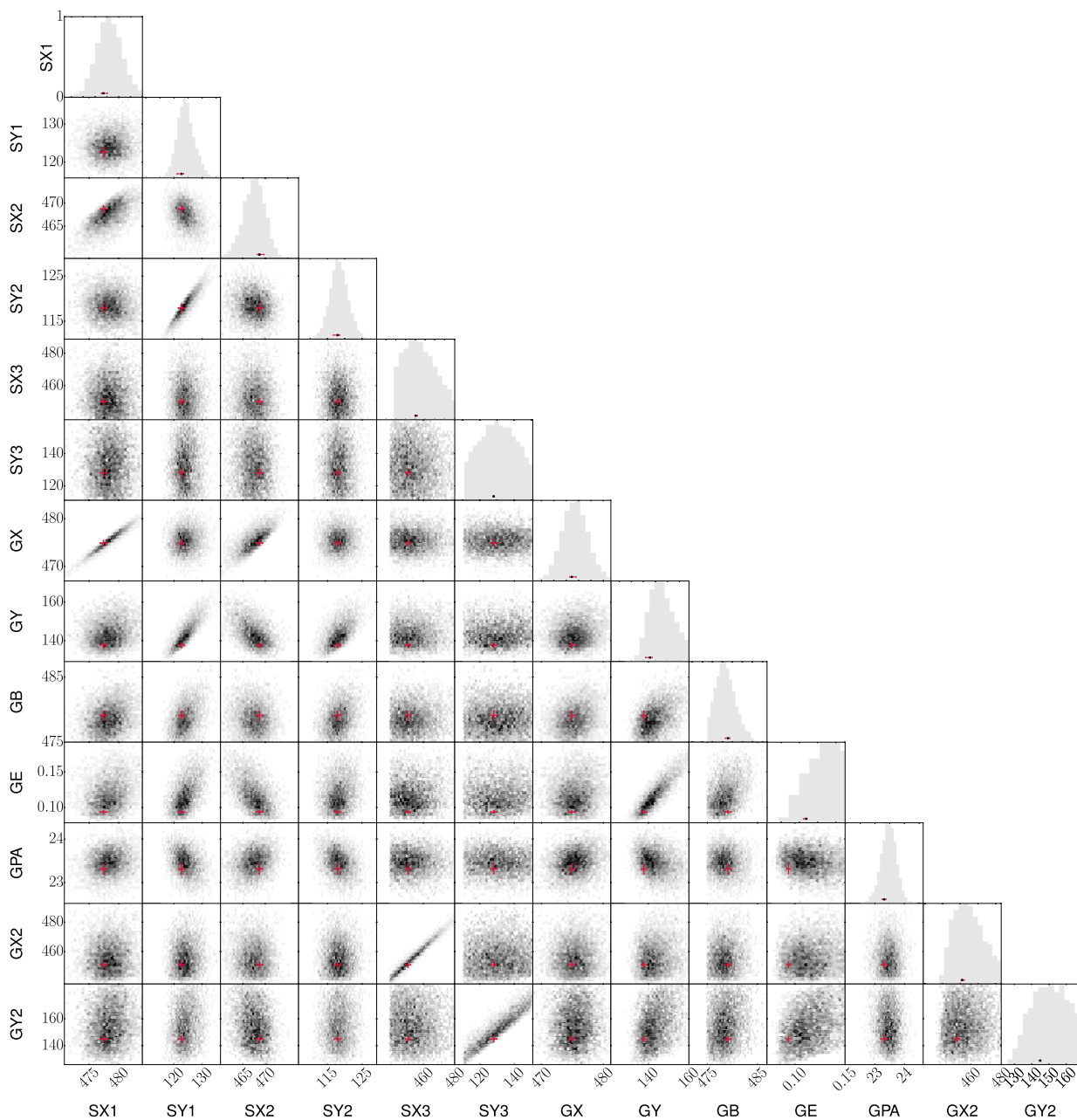
Figure 9. Posterior PDF plots for the parameters of the best-fitting model of HS 0810+2554 using positional constraints from the EVN image and *HST* observations. In each plot the error bars are centred on the mean and extend to the 3σ uncertainty values in the two-dimensional plots and to 1σ in the one-dimensional plots.

galaxy position angle of our model. The low shear in our model could therefore be explained by the degeneracy between ellipticity and shear, making it difficult to disentangle intrinsic and extrinsic shear when the two directions are almost identical.

Lensed image flux density values obtained from the model predict ratios greater than 10:1 between images of both sources forming in the general regions of A or B and images forming in the region of C. This prediction is discrepant with the observed flux density values, which find comparable values between images A, B, and C for both sources (Table 1). The apparently boosted flux density in region C could be the result of millilensing by dark matter substructure. However, the evidence from radio observations (Fig. 4) taken at other epochs shows that the relative flux density values between

all regions have varied over time-scales greater than 1 yr, implying that the cause of the discrepancy is due to intrinsic variation of the source: either the brightening and dimming of AGN activity, or the motion of jets across the plane of the lensing caustic.

Tables 3 and 5 report parameter estimates and predicted lensed image positions obtained using both EVN and *HST* observations. Fig 9 presents associated marginalized distribution plots. The tangential caustic and critical curves and the predicted and observed positions are plotted in Fig. 8. Adding the *HST* constraints allows us to predict a source configuration featuring the two radio components linearly aligned on either side of the optical quasar core (Fig. 6). Inclusion of *HST* positions also allows us to compare the separation between our galaxy position and *HST* component

A with the separation between observed *HST* galaxy position and observed component A. With respect to *HST* image A, RA and Dec. positions of the galaxy are predicted to be 456.5 ± 1.8 mas and 149.0 ± 1.9 mas, respectively, agreeing to within 1σ of the values reported in the CASTLES data base.

Magnification factors associated with each lensed image component were obtained by mapping the determinant of the lensing Jacobian used to perform ray tracing during the modelling process. Magnification is very strong in the region of images A and B, as would be expected in a merging fold system, and factors of 70, 46, 67, and 54 at the locations of A1, A2, B1, and B2, respectively, are found. These values are in fair agreement with a value of 50 from models of the narrow-line region made by Assef et al. (2011), and of 40 from models of X-ray emission made by Chartas et al. (2016), given the different locations of the various components in the high magnification regime next to the very small astroid caustic. Using the upper limit to the deconvolved source size of 1.55 mas from the EVN map, and assuming a standard flat cosmology with $\Omega_m = 0.27$ and $H_0 = 68 \text{ km s}^{-1} \text{ Mpc}^{-1}$, a conservative magnification factor of 50 gives an upper limit to the intrinsic component size in the source plane of just 0.27 pc. Furthermore, unresolved VLBI flux density measurements from the lensed plane at A1, A2, B1, and B2 imply an intrinsic source flux density no higher than 880 nJy at the source plane: the faintest radio source ever to be observed.

5 DISCUSSION AND CONCLUSIONS

The EVN observation of 0810+2554 provides the highest resolution image ever made of radio activity within an RQQ. The final map shows eight lensed components in total, and modelling of the system finds that the background source contains two highly compact components – one itself a double component – separated by $\sim$100 pc and positioned on the small astroid caustic. Intensity measurements find that only 37 ($\pm$4) per cent of flux density is lost as resolution is increased from the 220 mas scale to the 5 mas scale. Due to a resulting lensing magnification factor of $\sim$50, source structure can be seen on the sub-parsec scale, at a finer detail even than the closest unlensed quasars. 3C 273, for example, at a redshift of $z = 0.15$, can be resolved to a 3 pc scale at a resolution of 1 mas. The resolution of this observation finds each unresolved individual component to be no larger than 0.27 pc in diameter. The magnification factors also imply an intrinsic source flux density of just 880 nJy, making this object the faintest ever observed radio source and the first from the nJy regime.

The EVN map is complemented by observations using the e-MERLIN array at *C* band. Maps made at two different frequencies within the band allowed a relatively steep spectral index of $\alpha = -0.63 \pm 0.14$ to be measured, in agreement with the value found by Jackson et al. (2015). Further use of the unique combination of strong lensing with VLBI resolution and sensitivity allowed strong constraints to be placed on the brightness temperature of the radio components. Several authors, including Condon et al. (1991), Condon (1992), and Muxlow et al. (1994), place an upper limit on the brightness temperature of starburst regions, at 10^{4-5} K, although Condon et al. (1991) based this limit on observations made with a 0.25 arcsec resolution and therefore could not measure the brightness temperatures of sub-pc scale sources. With brightness temperature measurements that exceed 10^6 K, it appears very likely that the radio emission seen in HS 0810+2554 originates from AGN jet/core activity.

One alternative hypothesis is the possibility that the observed emission results from radio supernovae, which have been observed to display brightness temperatures in excess of 10^6 K and are very compact (Condon et al. 1991; Smith et al. 1998; Colina et al. 2001).

However, such sources vary over time-scales of $\sim$1 yr (Pietka, Fender & Keane 2015; Beswick 2006), both in flux density and in angular extent, and individual supernovae are likely to become resolved out by VLBI baselines over the time-scale since HS 0810+2554 was first observed.

It is possible that a high rate of supernova turnover in a starburst region could result in a compact area of consistently high brightness temperature. However, such regions generally occupy over 100–200 pc in extent, and the resolution of this observation would have revealed multiple such sources in the background plane, if present. For example, observations of strong nuclear activity within Arp 220 by Smith et al. (1998) found 12 radio supernovae within a 75×75 pc region, and Muxlow et al. (1994) found 40 supernova remnants distributed across the inner 700 pc of starburst galaxy M82. Compact AGN jets components, on the other hand, extend in a generally linear formation, occupying regions smaller than 0.1 pc near the quasar core (Junor, Biretta & Livio 1999).

In addition, following arguments also made by Blundell & Lacy (1995) in the study of closer, unlensed RQQ, the maximum supernova luminosity at radio frequencies is of order $\sim$$10^{21}$ W Hz^{-1} at 1.6 GHz (Rupen et al. 1987). Assuming a magnification factor of 50, the intrinsic flux density of HS 0810+2554 of 880 nJy yields a rest frame luminosity of 7.5×10^{21} W Hz^{-1} at redshift $z = 1.51$ using the derived spectral index of $\alpha = -0.63$. Therefore, tens of supernovae would be required to exist in three separate regions each smaller than the extent of the sub-parsec source component scale, in order for the observed flux density levels to be seen.

Our final piece of evidence comes from the inclusion of *HST* data as constraints to the lens model. This allowed the source reconstruction of three components – two radio and one optical – to be performed. The results show a clear linear alignment of the three background sources, with two opposing jet components situated very close to the quasar core. This presentation suggests the morphology of a compact symmetric object (CSO), in which compact jets are located on the parsec-scale either side of the core (Wilkinson et al. 1994; Owsianik, Conway & Polatidis 2001). Observations of the rapid advancement of hotspots in several CSOs suggest that CSOs represent a population of very young radio-loud sources, with ages under $\sim$1000 yr (Readhead et al. 1996; Owsianik & Conway 1998). Further observations have shown, however, that although some CSOs may evolve according to self-similar models into far larger and more luminous FR II objects, a large fraction are either short lived (An & Baan 2012) or produce recurrent small-scale jets (e.g. Owsianik, Conway & Polatidis 1998). The jets observed in HS 0810+2554 may therefore represent either the early stage of jet production within the AGN core or an intermittent type of lower power jet activity. It is important to note that, due to the finite scale of the strong lensing magnification region, our observations do not extend to the kpc scales typically associated with larger jet and lobe structure. We therefore cannot rule out the presence of such emission in this case.

By finding that even a quasar with the very faintest radio emission can contain jet activity, and that the radio emission from this activity can dominate the total radio output, this work provides direct evidence for a continuum model of jet production in the quasar population. It extends the work of Blundell et al. (1996), Blundell & Lacy (1995), and Blundell & Beasley (1998b), who have found similar evidence in sources of intermediate radio flux density. By imaging the radio emission morphology from a quasar of monochromatic radio luminosity $L_{1.6\,\text{GHz}} \sim 10^{22}$ W Hz^{-1}, it also suggests that the source count upturn at the faint end of the quasar luminosity function may not represent a population of different – star-forming – sources as suggested by Condon et al. (2013),

Padovani et al. ([2015](#)), and Kellermann et al. ([2016](#)). However, an investigation by Wucknitz & Volino ([2008](#)) found that a VLA and e-MERLIN detection of RQQ RX J1131−1231 was not replicated using VLBI, implying the absence of jets in this source. Larger studies of RQQs at high resolution will be required in order to determine the full contribution of jet-powered RQQs to the quasar luminosity function.

It is possible that jet production is able to coexist within RQQ alongside star-forming activity, with both phenomena triggered by the violent inflow of matter towards the SMBH. Stacey et al. ([2018](#)), for instance, studied a sample of gravitationally lensed quasars and found high levels of star formation in general, concluding that a coexistence of dust-obscured star formation and AGN activity is typical of most quasars. Several authors, e.g. Kewley et al. ([1999](#)) and Davies et al. ([2014](#)), have found starburst and AGN mixing in lower luminosity sources. These findings, along with the observations of HS 0810+2554, all suggest that jet activity does not represent a transitional stage of AGN activity but can feature at any stage of the AGN life cycle.

Of further significance is that the FIR luminosity measurements made by Stacey et al. ([2018](#)) found that HS 0810+2554 does not display the expected radio excess from the radio–FIR correlation typically associated with AGN activity. While we have found clear evidence for jet-dominated radio emission, observations of X-ray absorbing gas by Chartas et al. ([2014](#), [2016](#)) within HS 0810+2554 found evidence for a relativistic gas outflow. Since such ultrafast winds must originate from the active nucleus (Fabian [2012](#)), since AGN winds have been shown to contain heated dust (Baron & Netzer [2018](#)), and since the high dust temperature of this source is consistent with dust heated by the AGN (Weiß et al. [2007](#)), we suggest that the location of this source on the correlation may arise due to the coexistence of kinetic and radiative modes of AGN feedback. The radio–FIR correlation could therefore conceal emission processes other than star formation activity, and may not be a reliable method of distinguishing jetted from non-jetted quasars. This has already been suggested by Morić et al. ([2010](#)), who found that many AGN-dominated galaxies could not be separated from star-forming galaxies using their radio–FIR ratios alone and that the correlation can only be used reliably to separate a small fraction of the AGNs, such as the RLQs. The coexistence of jet activity and AGN winds also has implications for the understanding of AGN feedback modes within RQQ, for which radiation pressure is typically invoked over mechanical effects as the driving feedback mechanism (Wylezalek & Morganti [2018](#)).

RQQ PG 1115+080 has also been observed by Stacey et al. ([2018](#)). Again, a relatively high dust temperature has been measured, suggesting that the object lies, with HS 0810+2554, on the radio–FIR correlation of Ivison et al. ([2010](#)), yet X-ray observations by Chartas, Brandt & Gallagher ([2003](#)) have again found evidence for a relativistic gas outflow. We have recently conducted EVN observations of this additional source and will be able to access the correlated data shortly. VLBI detection of this object would again allow us to identify any bright and compact emission typical of an AGN, ruling out starburst activity as the primary mechanism at play. Detection of another jetted source in this region would demand an urgent review of the use of the correlation to classify star-forming and AGN activity.

Observations of HS 0810+2554 have also provided the opportunity to study the lensing galaxy itself. Modelling of the lens has suggested the presence of a non-smooth mass distribution in the vicinity of Einstein radius of image plane, producing astrometric perturbations of the compact VLBI lensed images. Our findings add to those of others (e.g. Biggs et al. [2004](#); Spingola et al. [2018](#))

who have been unable to fit smooth mass models to the data. We rule out the possibility of substantial baryonic disc structure since *HST* observations by Hsueh et al. ([2016](#)) find that the main lens appears to be an early-type elliptical galaxy. Relaxing the model to include the radial profile of the lens may reduce the positional offsets between the observed and modelled lensed components. However, studies by Chen et al. ([2007](#)) and Evans & Witt ([2003](#)) have found that using a simple smooth mass model rarely fits the data well. Instead, angular structure in the lens at different scales ranging from the SIE and down can reproduce observed offsets. Additionally, Keeton et al. ([1997](#)) have found that allowing the galaxy position, mass slope, and external shear of the macromodel to vary can mask intrinsic perturbations by an order of magnitude. More quantitative constraints on the possible presence of the substructures along the line of sight as derived from the astrometric anomalies suggested by our model of HS 0810+2554 will be presented in a forthcoming paper.

REFERENCES

An T., Baan W. A., 2012, ApJ, 760, 77
Argo M., 2015, preprint (arXiv:1502.04936)
Assef R. J. et al., 2011, ApJ, 742, 93
Baron D., Netzer H., 2018, MNRAS, 480, 2800
Bartelmann M., 2010, Class. Quantum Gravity, 27, 233001
Barvainis R., Lehár J., Birkinshaw M., Falcke H., Blundell K. M., 2005, ApJ, 618, 108
Belokurov V. et al., 2006, ApJ, 647, L111
Berdina L., Tsvetkova V. S. , 2018, Advances in Astronomy and Space Physics, 7, 12
Beswick R. et al., 2006, The 8th European VLBI Network Symposium, Proceedings of the 8th European VLBI Network Symposium, Proceedings of Science, Italy. p. 51
Biggs A. D., 2004, in Bachiller R., Colomer F., Desmurs J.-F., de Vicente P., eds, European VLBI Network on New Developments in VLBI Science and Technology, Proceedings of Science, Italy. p. 163
Biggs A. D., Browne I. W. A., Jackson N. J., York T., Norbury M. A., McKean J. P., Phillips P. M., 2004, MNRAS, 350, 949
Blundell K. M., Beasley A. J., 1998a, MNRAS, 299, 165
Blundell K. M., Beasley A. J., 1998b, MNRAS, 299, 165
Blundell K. M., Kuncic Z., 2007, ApJ, 668, L103
Blundell K. M., Lacy M., 1995, MNRAS, 274, L9
Blundell K. M., Beasley A. J., Lacy M., Garrington S. T., 1996, ApJ, 468, L91
Blundell K. M., Beasley A. J., Bicknell G. V., 2003, ApJ, 591, L103
Bonzini M., Padovani P., Mainieri V., Kellermann K. I., Miller N., Rosati P., Tozzi P., Vattakunnel S., 2013, MNRAS, 436, 3759
Bonzini M. et al., 2015, MNRAS, 453, 1079
Buchner J. et al., 2014, A&A, 564, A125
Chartas G., Brandt W. N., Gallagher S. C., 2003, ApJ, 595, 85
Chartas G., Hamann F., Eracleous M., Misawa T., Cappi M., Giustini M., Charlton J. C., Marvin M., 2014, ApJ, 783, 57

Chartas G., Cappi M., Hamann F., Eracleous M., Strickland S., Giustini M., Misawa T., 2016, ApJ, 824, 53

Chen J., Rozo E., Dalal N., Taylor J. E., 2007, ApJ, 659, 52

Claeskens J.-F., Sluse D., Riaud P., Surdej J., 2006, A&A, 451, 865

Colina L., Alberdi A., González-Delgado R., Torrelles J. M., Leitherer C., Panagia N., Wilson A. S., 2001, in Knapen J. H., Beckman J. E., Shlosman I., Mahoney T. J., eds, ASP Conf. Ser., Vol. 249, The Central Kiloparsec of Starbursts and AGN: The La Palma Connection. Astron. Soc. Pac., San Francisco, p. 119

Condon J. J., 1992, ARA&A, 30, 575

Condon J. J., Huang Z.-P., Yin Q. F., Thuan T. X., 1991, ApJ, 378, 65

Condon J. J., Kellermann K. I., Kimball A. E., Željko Ivezić Perley R. A., 2013, ApJ, 768, 37

Courbin F., Saha P., Schechter P. L., 2002, in Courbin F., Minniti D., eds, Lecture Notes in Physics, Vol. 608, Gravitational Lensing: An Astrophysical Tool. Springer-Verlag, Berlin, p. 1

Davies R. L., Rich J. A., Kewley L. J., Dopita M. A., 2014, MNRAS, 439, 3835

Dye S., Warren S. J., 2005, ApJ, 623, 31

Evans N. W., Witt H. J., 2003, MNRAS, 345, 1351

Fabian A. C., 2012, ARA&A, 50, 455

Fadely R., Keeton C. R., 2012, MNRAS, 419, 936

Feroz F., Hobson M. P., 2008, MNRAS, 384, 449

Feroz F., Hobson M. P., Bridges M., 2009, MNRAS, 398, 1601

Feroz F., Hobson M. P., Cameron E., Pettitt A. N., 2013, preprint (arXiv:1306.2144)

Garrett M. A., Calder R. J., Porcas R. W., King L. J., Walsh D., Wilkinson P. N., 1994, MNRAS, 270, 457

Graus A. S., Bullock J. S., Boylan-Kolchin M., Nierenberg A. M., 2017, MNRAS, 480, 1322

Greisen E., 2013, The AIPS Cookbook. NRAO, Charlottesville, VA

Herrera Ruiz N., Middelberg E., Norris R.P., Maini A., 2016, A&A, 589, L2

Homma D. et al., 2016, ApJ, 832, 21

Hsueh J.-W., Fassnacht C. D., Vegetti S., McKean J. P., Spingola C., Auger M. W., Koopmans L. V. E., Lagattuta D. J., 2016, MNRAS, 463, L51

Hsueh J.-W., Despali G., Vegetti S., Xu D., Fassnacht C. D., Metcalf R. B., 2018, MNRAS, 475, 2438

Ivison R. J. et al., 2010, A&A, 518, L31

Jackson N., 2011, ApJ, 739, L28

Jackson N., 2013, Bull. Astron. Soc. India, 41, 19

Jackson N. et al., 1998, MNRAS, 296, 483

Jackson N., Tagore A. S., Roberts C., Sluse D., Stacey H., Vives-Arias H., Wucknitz O., Volino F., 2015, MNRAS, 454, 287(J15)

Jullo E., Kneib J.-P., Limousin M., Elíasdóttir Á., Marshall P. J., Verdugo T., 2007, New J. Phys., 9, 447

Junor W., Biretta J. A., Livio M., 1999, Nature, 401, 891

Keeton C. R., Kochanek C. S., Seljak U., 1997, ApJ, 482, 604

Kellermann K. I., Sramek R., Schmidt M., Shaffer D. B., Green R., 1989, AJ, 98, 1195

Kellermann K. I., Condon J. J., Kimball A. E., Perley R. A., Ivezić Ž., 2016, ApJ, 831, 168

Kewley L. J., Heisler C. A., Dopita M. A., Norris R. P., 1999, Adv. Space Res., 23, 1045

Klypin A., Kravtsov A. V., Valenzuela O., Prada F., 1999, ApJ, 522, 82

Kochanek C. S., 2004, in Meylan G., Jetzer P., North P.,eds, The Sass Fee Lecture on Strong Gravitational Lensing, Gravitational Lensing: Strong, Weak & Micro, Proceedings of the 33rd Saas-Fee advanced course, Springer-Verlag, Berlin

Kochanek C. S., Dalal N., 2004, ApJ, 610, 69

Kochanek C. S., Falco E. E., Impey C. D., Lehár J., McLeod B. A., Rix H.-W., 1999, in Holt S., Smith E., eds, AIP Conf. Proc., Vol. 470, After the Dark Ages: When Galaxies were Young (the Universe at 2 < Z < 5). Am. Inst. Phys., New York, p. 163

Koopmans L. V. E., 2005, MNRAS, 363, 1136

Koopmans L. V. E., de Bruyn A. G., Wambsganss J., Fassnacht C. D., 2001, in Menzies J. W., Sackett P. D., eds, ASP Conf. Ser., Vol. 239, Microlensing 2000: A New Era of Microlensing Astrophysics. Astron. Soc. Pac., San Francisco, p. 363

Koopmans L. V. E. et al., 2003, ApJ, 595, 712

Koposov S.E., Belokurov V., Torrealba G., Evans N.W., 2015, ApJ, 805, 130

Laor A., Behar E., 2008, MNRAS, 390, 847

Laor A., Baldi R. D., Behar E., 2019, MNRAS, 482, 5513

Leipski C., Falcke H., Bennert N., Hüttemeister S., 2006, A&A, 455, 161

MacLeod C. L., Jones R., Agol E., Kochanek C. S., 2013, ApJ, 773, 35

Madau P., Dickinson M., 2014, ARA&A, 52, 415

Mao S., Schneider P., 1998, MNRAS, 295, 587

Metcalf R. B., Madau P., 2001, ApJ, 563, 9

Meylan G., Jetzer P., North P., Schneider P., Kochanek C. S., Wambsganss J., 2006, Gravitational Lensing: Strong, Weak and Micro, Springer-Verlag, Berlin,

Miettinen O. et al., 2017, A&A, 597, A5

Miller L., Kitching T. D., Heymans C., Heavens A. F., van Waerbeke L., 2007, MNRAS, 382, 315

Moller O., Hewett P., Blain A. W., 2003, MNRAS, 345, 1

Moore B., Ghigna S., Governato F., Lake G., Quinn T., Stadel J., Tozzi P., 1999, ApJ, 524, L19

Morić I., Smolčić V., Kimball A., Riechers D. A., Ivezić Ž, Scoville N., 2010, ApJ, 724, 779

Mosquera A. M., Kochanek C. S., 2011, ApJ, 738, 96

Mundell C. G., Wilson A. S., Ulvestad J. S., Roy A. L., 2000, ApJ, 529, 816

Muxlow T. W. B., Pedlar A., Wilkinson P. N., Axon D. J., Sanders E. M., de Bruyn A. G., 1994, MNRAS, 266, 455

Muxlow T. W. B. et al., 2005, MNRAS, 358, 1159

Nierenberg A. M. et al., 2017, MNRAS, 471, 2224

Orienti M., D'Ammando F., Giroletti M., Giovannini G., Panessa F., Bourke T.., 2015, Proc. Sci., The Physics of the Radio Emission in the quiet side of the AGN population with the SKA, SISSA, Trieste, (PoS(AASKA14)087)

Owsianik I., Conway J. E., 1998, A&A, 337, 69

Owsianik I., Conway J. E., Polatidis A. G., 1998, A&A, 336, L37

Owsianik I., Conway J., Polatidis A., 2001, in Schilizzi R. T., ed., Proceedings of The International Astronomical Union, Proceedings of Science, Italy, p. 205

Padovani P., 2017, Nat. Astron., 1, 0194

Padovani P., Bonzini M., Kellermann K. I., Miller N., Mainieri V., Tozzi P., 2015, MNRAS, 452, 1263

Phillips P. M. et al., 2000, MNRAS, 319, L7

Pietka M., Fender R. P., Keane E. F., 2015, MNRAS, 446, 3687

Readhead A. C. S., Taylor G. B., Pearson T. J., Wilkinson P. N., 1996, ApJ, 460, 634

Reimers D., Hagen H.-J., Baade R., Lopez S., Tytler D., 2002, A&A, 382, L26

Ritondale E., Vegetti S., Despali G., Auger M. W., Koopmans L. V. E., McKean J. P., 2018, in press

Rupen M. P., van Gorkom J. H., Knapp G. R., Gunn J. E., Schneider D. P., 1987, AJ, 94, 61

Rusin D., Norbury M., Biggs A. D., Marlow D. R., Jackson N. J., Browne I. W. A., Wilkinson P. N., Myers S. T., 2002, MNRAS, 330, 205

Schmidt M., 1963, Nature, 197, 1040

Serjeant S., 2012, MNRAS, 424, 2429

Sluse D., Chantry V., Magain P., Courbin F., Meylan G., 2012, A&A, 538, A99

Smith H. E., Lonsdale C. J., Lonsdale C. J., Diamond P. J., 1998, ApJ, 493, L17

Sonnenfeld A., Treu T., Gavazzi R., Marshall P. J., Auger M. W., Suyu S. H., Koopmans L. V. E., Bolton A. S., 2012, ApJ, 752, 163

Sonnenfeld A., Treu T., Gavazzi R., Suyu S. H., Marshall P. J., Auger M. W., Nipoti C., 2013, ApJ, 777, 98

Sonnenfeld A., Treu T., Marshall P. J., Suyu S. H., Gavazzi R., Auger M. W., Nipoti C., 2015, ApJ, 800, 94

Sopp H. M., Alexander P., 1991, MNRAS, 251, 14P

Spingola C., McKean J. P., Auger M. W., Fassnacht C. D., Koopmans L. V. E., Lagattuta D. J., Vegetti S., 2018, MNRAS, 478, 4816

Stacey H. R. et al., 2018, MNRAS, 476, 5075

Suyu S. H., Marshall P. J., Hobson M. P., Blandford R. D., 2006, MNRAS, 371, 983

Treu T., Koopmans L. V. E., 2002, ApJ, 575, 87
Treu T., Koopmans L. V. E., 2003, MNRAS, 343, L29
Treu T., Koopmans L. V. E., 2004, ApJ, 611, 739
Ulvestad J. S., Ho L. C., 2001, ApJ, 562, L133
Vegetti S., Koopmans L. V. E., Bolton A., Treu T., Gavazzi R., 2010, MNRAS, 408, 1969
Vegetti S., Lagattuta D. J., McKean J. P., Auger M. W., Fassnacht C. D., Koopmans L. V. E., 2012, Nature, 481, 341
Warren S. J., Dye S., 2003, ApJ, 590, 673
Weiß A., Downes D. , Neri R., Walter F. , Henkel C., Wilner D. J., Wagg J., Wiklind T., 2007, A&A, 467, 955
White S. V., Jarvis M. J., Kalfountzou E., Hardcastle M. J., Verma A., Cao Orjales J. M., Stevens J., 2017, MNRAS, 468, 217
Wilkinson P. N., Polatidis A. G., Readhead A. C. S., Xu W., Pearson T. J., 1994, ApJ, 432, L87

Wisnioski E., Glazebrook K., Blake C., Poole G. B., Green A. W., Wyder T., Martin C., 2012, MNRAS, 422, 3339
Wucknitz O., Volino F., 2008, Proc. Sci., The gravitational lens J1131–1231 — How to avoid missing an opportunity, SISSA, Trieste, (PoS(IX EVN Symposium)102)
Wylezalek D., Morganti R., 2018, Nat. Astron., 2, 181
Xu D., Sluse D., Gao L., Wang J., Frenk C., Mao S., Schneider P., Springel V., 2015, MNRAS, 447, 3189
Zackrisson E., Riehm T., 2010, Adv. Astron., 2010, 478910
Zackrisson E. et al., 2013, MNRAS, 431, 2172
Zakamska N. L., Greene J. E., 2014, MNRAS, 442, 784
Zakamska N. L. et al., 2015, MNRAS, 455, 4191
Zucker D. B. et al., 2006, ApJ, 643, L103

APPENDIX : EVN 1.6 GHz MAP OF HS 0810+2554

A contour plot is provided in order to show the uncovered background.
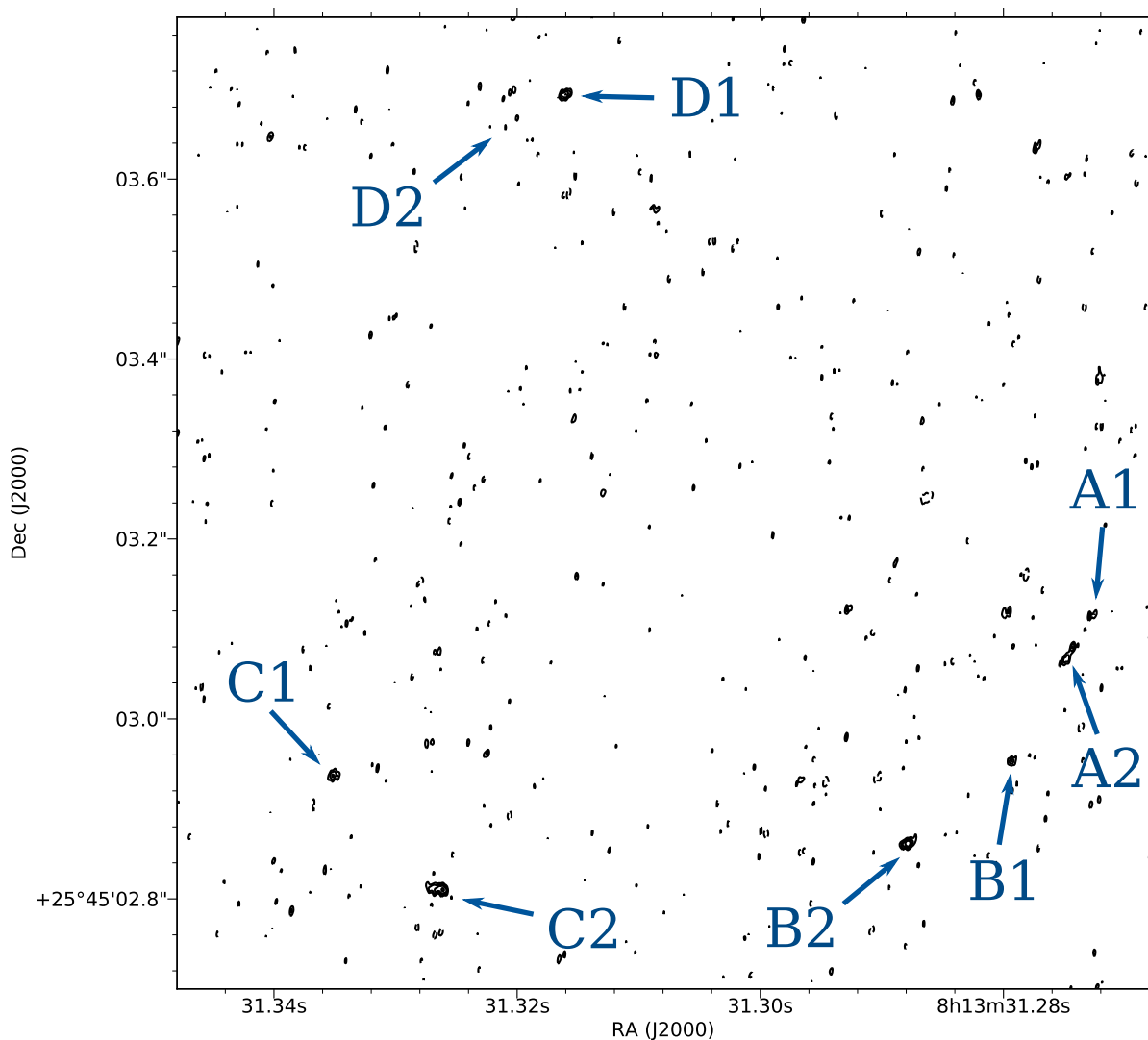

Figure A1. EVN image of HS 0810+2554 at 1.65 GHz produced using a natural weighting scheme. The contours are drawn at $(-3, 3, 4, 5, 6) \times 7.2$ μJy. The peak surface brightness is 52 μJy beam^{-1}, at component B2. The beam is at FWHM at 12.0×8.5 mas at a position angle of $-3°$.

This paper has been typeset from a TeX/LaTeX file prepared by the author.